Journal of Constructional Steel Research 198 (2022) 107569

Contents lists available at ScienceDirect

Journal of Constructional Steel Research

journal homepage: www.elsevier.com/locate/jcsr

Effective material model for cold-formed rectangular hollow sections in beam element-based advanced analysis

Lauri Jaamala [a,*], Kristo Mela [a], Juha Tulonen [b], Anssi Hyvärinen [b]

[a] Tampere University, Tekniikankatu 12, 33720 Tampere, Finland
[b] SSAB, Harvialantie 420, Hämeenlinna 13300, Finland

ARTICLE INFO

Keywords:
Advanced design method
Cold-formed
High-strength steel
Buckling
Residual stress, corner strength enhancement

ABSTRACT

This study develops and validates an effective material model for cold-formed rectangular hollow sections. Advanced design methods utilize non-linear finite element analysis in design. An accurate calculation model, which is usually beam element-based, is crucial such that the design outcome is safe but economical. Unfortunately, cold-formed sections have non-linear residual stress distribution over the material thickness, that cannot be explicitly modelled in general-purpose beam elements. Additionally, corner regions of cold-formed sections have higher material strength compared to flat regions. This beneficial feature is usually disregarded by assuming the flat region properties for the entire cross-section. This study develops an effective material model that replicates a stress-strain curve that would be obtained if the tensile test was made for the entire cross-section instead of a separate tensile coupon. Consequently, the effects of residual stresses and corner strength enhancements are included in the effective material model such that their consideration in beam element-based advanced design method is effortless. The effective material model is validated for the steel grade S700 against numerical shell element buckling tests and excellent modelling accuracy is achieved.

1. Introduction

The utilization of Nonlinear Finite Element Analysis (NFEA) as a design tool is drawing more attention due to the fast development of computers and commercial FEM packages. In Eurocode 3 [1], [2], this type of Advanced Design Method (ADM) is termed GMNIA, which stands for **G**eometrically and **M**aterially **N**onlinear **I**mperfection **A**nalysis. In Australian and New Zealand standard AS/NZS 4600:2018 [3] such a method is termed "Advanced Analysis" or "GMNAI".

Usually, beam elements are employed in ADM because of their computational efficiency. Unfortunately, using beam elements causes challenges for modelling the cross-sectional properties of cold-formed rectangular hollow sections (CFRHS). These challenges are due to effects of cold-forming on the material properties of the cross-section. In many commercial finite element packages such as in Abaqus [4], the cross-section of a general-purpose beam element can comprise of one material. However, cold-forming causes strength enhancements, and especially corner regions of CFRHS have higher yield and ultimate strengths compared to the flat regions of the cross-section [5], [6]. Hence, multiple material models would be needed to utilize these strength enhancements in the capacity calculations. Cold forming induces also residual stresses, which vary nonlinearly through the thickness of the material [7]. Cross-sections of thin-walled hollow section beam elements usually have only one integration point in the thickness direction of the material. A single integration point is not capable of describing the varying residual stress distribution through the thickness. Because of these limitations in general-purpose beam elements, the direct modelling of varying material properties and residual stresses is not possible, and approximation method is needed.

An often-employed approach to account for geometrical and material imperfections (including residual stresses) is to use so-called "equivalent geometrical imperfections" (EGI), as presented, for example in Eurocode 3 [1]. By using EGI, all relevant imperfections can be modelled with a single out-of-straightness (bow) imperfection e_1 shown in Fig. 1. Magnitudes defined for EGI have been criticized to be both unsafe or overly conservative for inelastic analyses depending on the shape and material of the cross-section, and these magnitudes have been recently refined [8], [9].

The utilization of EGI is a simple and computationally efficient approximation method. However, it has one fundamental shortcoming that has been already identified in the literature: Results of Batterman and Johnston [10] and Bjorhovde [11] show that *the separate effects of*

* Corresponding author.
E-mail address: lauri.jaamala@tuni.fi (L. Jaamala).

https://doi.org/10.1016/j.jcsr.2022.107569
Received 1 August 2022; Received in revised form 14 September 2022; Accepted 15 September 2022
Available online 26 September 2022

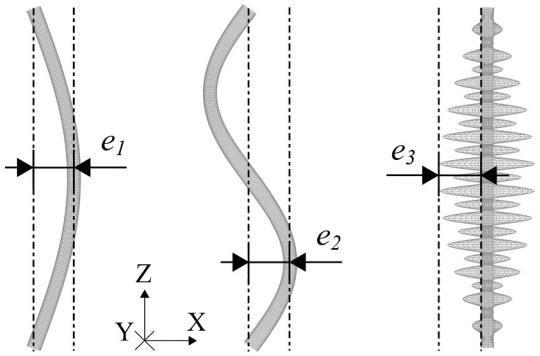

Fig. 1. Shapes of geometrical imperfections e_1, e_2 and e_3.

residual stresses and initial out-of-straightness cannot be added to give a good approximation of the combined effect on the maximum column strength. In some cases, and for some slenderness ratios, the combined effect is less than the sum of the parts (intermediate slenderness ratios, low residual stresses). In other cases the combined effect is more than the sum of the parts (citation from Ziemian [12]). A structure can be sensitive or insensitive to geometrical imperfections, hence the effects of residual stresses in such structures will be over- or underestimated when employing EGI.

An alternative approximation method, which considers the residual stresses by reducing the stiffness of the stress-strain curve of the material, has been presented in the literature [13], [14]. This stiffness reduction method yields an equally simple procedure as the use of EGI, but the shortcoming of EGI for imperfection insensitive structures is avoided by considering the effects of residual stresses in the material model. Although the stiffness reduction method has been already in use [15], the authors have not found any studies that validate the accuracy of the method.

To consider the corner strength enhancement and the effects of residual stresses in a beam element-based advanced analysis, this study presents an effective material model (EMM) for CFRHS structures, which is applied on steel grade S700. The EMM is a weighted average from the flat part and corner region materials, that also contains the effects of residual stresses according to the stiffness reduction method. The accuracy of the EMM is validated by comparing the global buckling capacities of beam element-based EMM models to shell element models in which the residual stresses are explicitly modelled. Validation is made for isolated columns and beam-columns with various cross-section sizes, non-dimensional slenderness ratios, and boundary conditions. Additionally, Monte Carlo-simulations [16] for the global buckling analysis are carried out for varying material, geometrical and residual stress properties to validate the applicability of EMM to reliability studies, which are a central component of determining the safety factors of ADMs [15]. Monte Carlo-simulations require accurate statistical distributions for the cross-sectional properties. Therefore, these distributions are considered in the same level of detail as in actual reliability analysis. As an outcome of this study, a convenient EMM approach is proposed that can be used for modelling of CFRHS in ADMs and reliability studies in future research.

2. Residual stresses of cold-formed rectangular hollow sections

Residual stresses can have a significant impact on the global buckling capacity of compressed steel members [12], thus their effects must be considered in ADM. In this study, residual stresses are treated as presented in [7]. In the following, the assumed distributions of the relevant stress components are briefly provided, more details can be found in [7].

Of the various residual stress components, only the longitudinal and transversal bending components, σ_{LB} and σ_{TB}, respectively, are assumed to have a significant effect on the global buckling capacity, and the remaining components are neglected [6], [7], [17], [18]. The distributions of σ_{LB} and σ_{TB} along the cross-section perimeter and through the thickness are shown in Fig. 2. Fig. 3 presents the cross-sectional points CC (center of corner), NC (near corner) and MP (mid-plate) along the perimeter s for 1/4th of a cross-section. NC is the point at which the outer corner radius R_o and flat part intersect. Residual stress distribution and cross-sectional points are symmetrical with respect to axes 1–1 and 2–2 of Fig. 3.

Residual stresses at the location s along the perimeter (see Fig. 3) are obtained by:

$$\sigma_i(s) = \chi_j(s) \bullet \sigma_j \tag{1}$$

where i is L or T and j is LB or TB. σ_{TB} is constant along the perimeter s such that the residual stress distribution $\sigma_{TB,Flat}$ in the flat region MP-NC is used also in the corner region CC-NC (see Fig. 2). σ_{LB} however, is divided into $\sigma_{LB,Flat}$ (MP-NC) and $\sigma_{LB,Corner}$ (NC-CC), thus distinguishing the variations in the magnitude of longitudinal residual stresses in the corner and in the flat region. Relative through-thickness residual stress distributions of Fig. 2 are obtained by the formulae:

$$\sigma_{LB,Flat}(f_y) = -7.694 \bullet 10^{-7} f_y^2 + 6.737 \bullet 10^{-4} f_y + 0.562 \left[1/f_y\right] \tag{2}$$

$$\sigma_{LB,Corner}(f_y) = -4.757 \bullet 10^{-7} f_y^2 + 2.161 \bullet 10^{-4} f_y + 0.548 \left[1/f_y\right] \tag{3}$$

$$\sigma_{TB,Flat}(f_y) = \begin{cases} -2.339 \bullet 10^{-7} f_y^2 + 7.613 \bullet 10^{-5} f_y + 0.324, \text{for} f_y \le 960\,\text{MPa} \\ 0.181, \text{for} f_y > 960\,\text{MPa} \left[1/f_y\right] \end{cases} \tag{4}$$

where f_y is the yield stress of the flat region of CFRHS in MPa. Outcomes of Eqs. (2)–(4) are residual stress magnitudes relative to the yield stress of the flat region of the member, $[1/f_y]$. Hence, the actual residual stresses are obtained by multiplying the relative residual stresses by the flat region yield stress.

3. Material model for high-strength steel

Ramberg-Osgood model [19] is typically used to describe the rounded stress-strain curve of high-strength steels (HSS) [20]. This study adopts a two-stage model presented by Gardner and Yun [21]. The stress-strain relationship of the model is obtained by:

$$\varepsilon(f) = \begin{cases} \dfrac{f}{E} + 0.002\left(\dfrac{f}{f_y}\right)^n, \text{for} f \le f_y \\ \dfrac{f - f_y}{E_{0.2}} + \left(\varepsilon_u - \varepsilon_{0.2} - \dfrac{f_u - f_y}{E_{0.2}}\right)\left(\dfrac{f - f_y}{f_u - f_y}\right)^m + \varepsilon_{0.2}, \text{for} f_y < f \le f_u \end{cases} \tag{5}$$

where the first strain hardening exponent n, tangent modulus at the yield strength $E_{0.2}$, the minimum strain ε_u at ultimate tensile strength f_u, and the second strain hardening exponent m can be obtained by:

$$n = \frac{ln4}{ln\left(f_y/\sigma_{0.05}\right)} \tag{6}$$

$$E_{0.2} = \frac{E}{1 + 0.002n\frac{E}{f_y}} \tag{7}$$

$$\varepsilon_{u,lower\ bound} = \varepsilon_{0.2} + \frac{f_u - f_y}{E_{0.2}} \tag{8}$$

$$\varepsilon_u = max\left(\varepsilon_{u,lower\ bound},\ \varepsilon_u \text{ acc. to Table 1 (flat) or Table 3 (corner)}\right) \tag{9}$$

$$m = 1 + 3.3\frac{f_y}{f_u} \tag{10}$$

where f_y is the yield stress (0.2% proof stress for HSS) and $\sigma_{0.05}$ is the 0.05% proof stress. Model parameters for the flat region material are

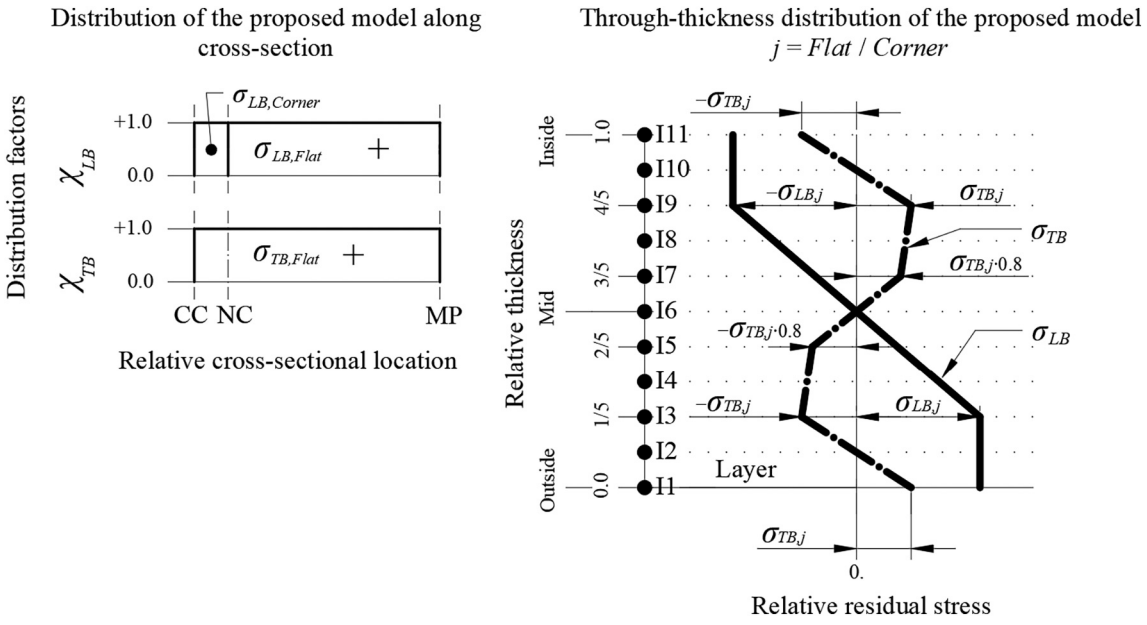

Fig. 2. Residual stress distribution for CFRHS [7].

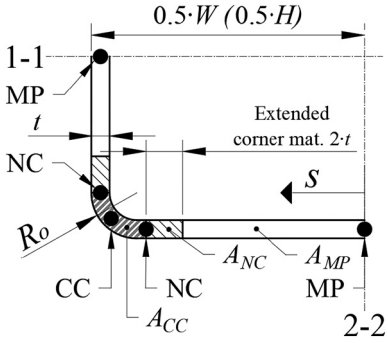

Fig. 3. 1/4th of a cross-section and location of points MP, NC, and CC.

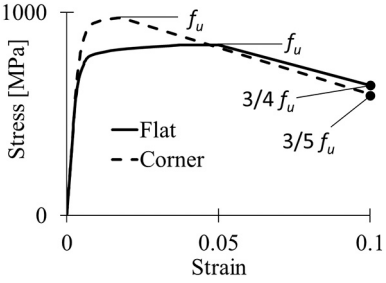

Fig. 4. The stress-strain curves of the flat and corner materials.

shown in Table 1, and the obtained stress-strain curve is plotted in Fig. 4. Except for the elastic modulus E, these parameters are determined based on the dataset obtained from the manufacturer of CFRHS (DSet). DSet included measurements from flat parts of grade S700 CFRHS members governing a wide range of width-to-thickness ratios. The $\sigma_{0.05}$ was determined based on 144 measured stress-strain curves and f_y, f_u and ε_u on 271 recorded tensile coupon test readings. It should be noted that the mean stress values f_y, f_u and $\sigma_{0.05}$ presented in Table 1 are the mean mill test values multiplied by a factor of 0.9965 [20]: Strain rates in the tensile tests may be higher than in the actual loading situation leading to higher measured stresses, hence it is recommended to reduce the measured mill test readings in reliability studies [16], [22]. However, in the case of HSS and testing based on stress rate (method B in [23]), the reduction factor is minor [20]. This condition corresponds to measurements of DSet and is applied in this study. It should also be noted that ε_u is determined according to the measured value but the lower bound in Eq. (8) ensures appropriate strain values in the two-stage material model. The modulus of elasticity E cannot be properly determined from the usual uniaxial tensile test [23], [22], hence its parameters are based on a draft of prEN 1993-1-1 [24].

The enhanced corner material is assumed to extend by the distance 2 t from NC into the flat region (t is the wall thickness of the cross-section) [25–29], as shown in Fig. 3. Based on two unpublished and 10 published measurements taken from S700 CFRHS [6], [30], [31], the corner strength enhancement factors C_{fy} and C_{fu} are calculated according to the equations in Table 2. Additionally, the ε_u of the corner material is assumed to be 1.7% on average [6], and 2.5% at maximum in Monte Carlo-simulations. Table 3 summarizes the selected corner material parameters.

It should be noted that the two-stage material model is valid up to the stress f_u and strain ε_u. For the flat material, it is assumed in this study that a constant yield plateau remains up to the strain 5%, after which the stress decreases linearly to the level of 3/4 of f_u at strain 10%, see Fig. 4.

Table 1
Material parameters for the flat region of the grade S700 steel.

Property	Description	Distribution	Mean	COV [%]	Ref.
f_y	Yield strength	Normal	746.5 MPa	2.76	DSet
f_u	Ultimate strength	Normal	839.5 MPa	2.47	DSet
$\sigma_{0.05}$	0.05% proof stress	Normal	641.9 MPa	5.47	DSet
ε_u	Strain at f_u	Normal	0.037	25.18	DSet
E	Elastic modulus	Normal	210 GPa	3.00	[24]
ν	Poisson's ratio	Deterministic	0.3	–	[1]

Table 2
Corner strength enhancement factors.

Property	Description	Distribution	Mean	COV [%]
C_{fy}	Corner strength enhancement factor for f_y and $\sigma_{0.05}$	Student's t	1.21	6.74
C_{fu}	Corner strength enhancement factor for f_u	Full correlation with C_{fy}	$C_{fu} = 0.35 \bullet C_{fy} + 0.74$	

Table 3
Material parameters for the corner and near corner regions of the grade S700 steel.

Property	Value
f_y	$C_{fy} \bullet f_y$ of the flat region
f_u	$C_{fu} \bullet f_u$ of the flat region
$\sigma_{0.05}$	$C_{fy} \bullet \sigma_{0.05}$ of the flat region
ε_u	1.7%
E	E of the flat region
ν	ν of the flat region

The stress decrease in the material model accounts for the necking phenomenon, which is not explicitly modelled at the element level. For the corner material, a constant yield plateau having the length of 0.1% strain is assumed after ε_u, and subsequently, the linear stress decrease to 3/5 of f_u is assumed at strain 10%. These limits were determined conservatively based on the stress-strain curves of the flat region (DSet) and corner region ([6]). However, global buckling usually occurs at strains below ε_u, thus these limits are of secondary importance.

4. Effects of residual stresses and elastic modulus on the stress-strain curve

In the literature, two approaches for treating residual stresses of CFRHS in computational models have been employed: Some authors incorporate the longitudinal bending residual stress σ_{LB} into the calculation models [32–34], whereas others assume that the effects of the σ_{LB} are inherently incorporated in the measured stress-strain curve of the material [35], [29], [28]. The latter is based on the idea that the σ_{LB} is approximately reintroduced to the tensile coupon when fastening it to the friction grips of a tensile testing machine [36].

At least two possible sources of error may be present when assuming that the effects of σ_{LB} are already incorporated into the measured stress-strain curve: (1) If plastic deformation occurs in straightening the tensile coupon for the grips of the testing machine, the original residual stress distribution will not be reintroduced [35]; (2) if residual stresses decrease the elastic modulus, but instead of the actual measured elastic modulus, some general value, e.g., $E = 210$ GPa, is used in the analysis. The effects of residual stresses and elastic modulus on the stress-strain curve are illustrated as follows:

1. Fig. 5 presents the average stress-strain curve of DSet (data from manufacturer), denoted "*Measured*". The curve is modelled according to the two-stage Ramberg-Osgood model presented in Section 3 (Eq. (5)), having the elastic modulus as the measured mean $E \approx 200$ GPa and the remaining parameters as the mean values of Table 1.
2. The 0.2% proof stress f_y can be determined from the intersection of the stress-strain curve and a line positioned at strain 0.002 shown as point P_0 in Fig. 5. The slope of the line, ≈200 GPa, is determined by linear regression from measured data points between ≈10% and ≈40% of the f_y [23]. Similarly, the stress $\sigma_{0.05}$ at point P_1 can be determined.
3. The modulus of elasticity obtained from the uniaxial tensile test is not accurate, because many sources of error exist in the measurement situation, such as misalignment of the test piece [23], [22]. Therefore, usually, e.g., $E = 210$ GPa is assumed for carbon steels [1]. By assuming $E = 210$ GPa instead of $E = 200$ GPa, the *Measured* curve is converted to the curve denoted "*Selected*", see Fig. 5. Consequently, *Selected* has Δ_E higher stress at P2 than *Measured*. If residual stresses have decreased the elastic modulus of the measured stress-strain curve and it is supposed that residual stresses are already included in the curve, the assumption that $E = 210$ GPa may be unconservative with respect to initial stiffness and stress magnitudes (see P1 vs. P2 in Fig. 5).
4. In NFEA, a numerical tensile test can be performed without misalignment and other sources of errors, which allows solving the contribution of residual stresses in the elastic modulus. Therefore, a standard tensile test coupon having thickness of 5 mm, width of 20 mm and length of 71.5 mm [23] was modelled by solid elements and tensioned utilizing NFEA. The coupon had a material model according to *Selected* of Fig. 5. Additionally, 70% of the longitudinal bending residual stress of the flat region (Eq.(2)), i.e. $\sigma_{LB} = 0.7 \bullet 0.64 \bullet 746.5$ MPa $= 332$ MPa, was introduced for 10 layers of solid elements in the through-thickness direction according to the model of Fig. 2. Magnitude of 70% represents the average amount of σ_{LB} that is not included in the measured stress-strain curve (see Section 5). As a result of this NFEA "tensile test", the curve denoted "*Selected + 70%*" in Fig. 5 is obtained.
5. The elastic modulus determined by linear regression (as in Item 2) of the curve *Selected + 70%* is ≈200 GPa and $\sigma_{0.05}$ is at P_3. This curve contains no measurement uncertainties of the real world, hence it is evident that the σ_{LB} has reduced E by 10 GPa ($E = 210$ GPa in *Selected* in NFEA) and $\sigma_{0.05}$ by Δ_{RS} (from P_1 to P_3).
6. By imagining the above situation at P_0 when determining f_y, it is obvious that the obtained stress-strain curves are more closely bundled together, and no such large stress differences exist. Therefore, residual stresses affect especially the elastic modulus and $\sigma_{0.05}$, and not much of f_y.

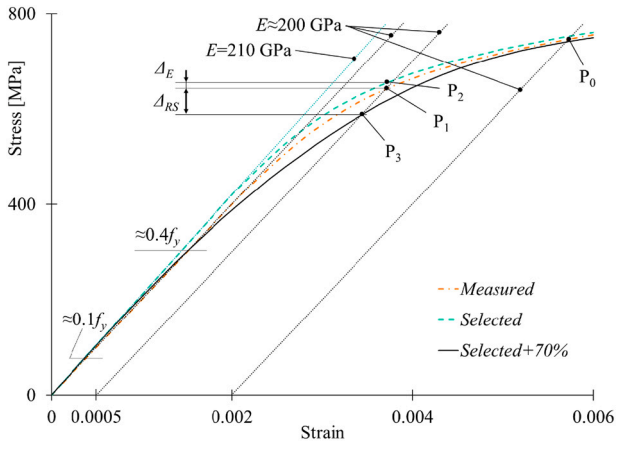

Fig. 5. The effects of E and σ_{LB} on the stress-strain curve (Measured: E = measured ≈ 200 GPa; Selected: $E = 210$ GPa; Selected+70%: $E \approx 200$ GPa due to σ_{LB}).

The actual magnitudes of Δ_E and Δ_{RS} depend on the residual stress level, measurement errors of the elastic modulus and the shape of the stress-strain curve in general (rounded as for HSS or bilinear as for normal strength steel). In this study, residual stresses are incorporated into NFEA in conjunction with the mean $E = 210$ GPa. Consequently, the increase Δ_E, but additionally the decrease Δ_{RS} by σ_{LB} will be considered.

5. Magnitude of σ_{LB} in the measured stress-strain curve

Even if the stress-strain curve with the measured elastic modulus was used in the ADM instead of $E = 210$ GPa, the outcome can be unsafe if the σ_{LB} has not been reintroduced to the tensile coupon. To evaluate to which extent the effects of σ_{LB} have been incorporated into the measured stress-strain curves, NFEA tensile tests presented in Item 4 of Section 4 were carried out for the following material models:

1. Curve *Selected* in Fig. 5 is also presented in Fig. 6. By carrying out the NFEA tensile test with the material model *Selected* and incorporating 100% of σ_{LB} according to the residual stress model, the curve "*Selected + 100%*" is obtained. This curve can be regarded as an upper bound for the effects of σ_{LB} because it contains the possible

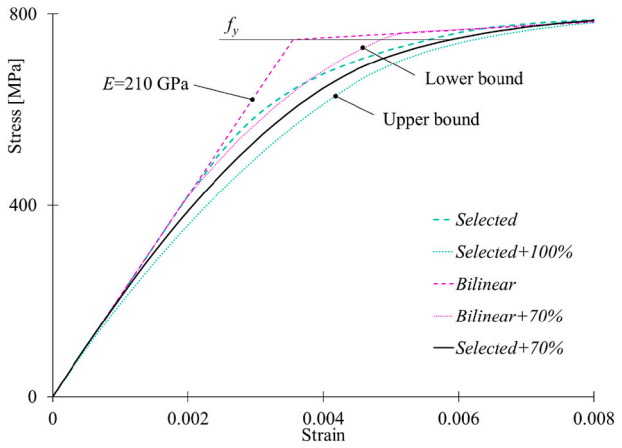

Fig. 6. The magnitude of σ_{LB} in the measured stress-strain curve.

effects of σ_{LB} in the used material model, and additionally, the full residual stress pattern of σ_{LB} is incorporated.

2. The residual stress model [7] is presumably conservative: The in-situ residual stress measurements obtained by the sectioning method correspond to linearly varying stress distribution through the thickness. When the nonlinear through-thickness distribution is assumed as for σ_{LB} in Fig. 2, the measured linearly varying stresses can be multiplied by 9/13 ≈ 70% to convert the linear distribution to nonlinear [17]. This is justified since the sectioned coupon is not free from stresses, thus the measured surface stresses of the released coupon do not represent the actual residual stresses. The residual stress model [7] is heavily based on the measurements obtained by the sectioning method, but the reduction of 9/13 has not been considered in the model due to uncertainty because of limited research data.

   Consider now an imaginary material model "*Bilinear*", which is fully elastic up to f_y, and which has slight strain hardening such that the material model coincides with the other material models at strain 0.008. By carrying out the NFEA tensile test with the material model *Bilinear* and incorporating 70% of σ_{LB}, a curve "*Bilinear + 70%*" is obtained. This curve can be regarded as a lower bound for the cumulative effects of σ_{LB} and rounded stress-strain curve because the material model is very unconservative in terms of stiffness for HSS and contains absolutely no effects of residual stresses. It is worth noting that *Bilinear + 70%* has the measured elastic modulus of 209 GPa obtained by linear regression, i.e., almost the same as in the base material model *Bilinear*, 210 GPa. Therefore, the issues concerning the selection of elastic modulus (Fig. 5) are especially relevant for HSS which has a rounded stress-strain curve, and the impact on normal strength steels may be small depending on the shape of the stress-strain curve.
3. The curve "*Selected + 70%*" of Fig. 5 is presented also in Fig. 6. This curve is a somewhat average curve for lower and upper bound curves *Bilinear + 70%* and *Selected + 100%*. Therefore, in this study, it is assumed that 30% of the effects of σ_{LB} have been already incorporated into the material model and 70% of the σ_{LB} will be incorporated explicitly into calculation models.

6. Effective material model

The effective material model (EMM) provides a material model applicable to beam elements that emulates the stress-strain curve that would be obtained if the tensile test was carried out for the full cross-section of a CFRHS member. The stress-strain curve based on a tensile test on full cross-sections includes inherently the combined effects of residual stresses and strength enhancements of the corner material. In practice, the EMM can be generated by modelling the entire cross-section with shell or solid elements including residual stresses and by applying a tension load to the cross-section in NFEA.

In Monte Carlo-simulations, thousands of EMMs are needed for various cross-section sizes, material parameters, and residual stress magnitudes. To effectively generate these EMMs, a Matlab [37] script was programmed. The script performs nonlinear finite element analysis with two solid elements: Fig. 7 presents two isoparametric three-dimensional hexahedral elements, having 8 nodes and three degrees of freedom (DOF) per node for each element. The global X-axis of the figure is in the direction of the longitudinal axis of the member and Z-axis in the thickness direction of the material. Boundary conditions of nodes N1-N12 are presented in Table 4. Nodes of each side, e.g., nodes of faces 1 and 2, are coupled with multipoint constraints (MPC) such that all nodes translate within the current plane XY, XZ or YZ. MPCs ensure that the finite material element, which is described by these 2 solids, behaves like a real material element in a cross-section that is surrounded by the rest of the cross-section material. NFEA tensile test can be performed by applying a force F to the nodes of face 1 and formulating the "measured" stress-strain curve from the recorded total applied forces and X-displacements of face 1.

Two solids are not capable of describing the entire material thickness of a CFRHS, because bending residual stresses are varying according to Fig. 2 such that at least 5 equally thick layers (solids) through the thickness would be needed. However, using only two solid elements is selected in this study to facilitate the implementation. EMMs over the entire cross-section thickness can be generated with these two solid elements by combining the results of multiple analyses:

1. Divide the cross-section into 11 separate layers between the integration points I1-I11 as shown in Fig. 8. Integration points I1 and I11 are positioned at the surfaces of the material to make the integration scheme match Simpson's rule used in shell elements. Note that locations of the integration points I1-I11 are identical between Figs. 8 and 2, but layer division differs: in Fig. 2, the through-thickness direction was divided into 10 layers (instead of 11), which corresponds to the division for 10 solid elements as used in Item 4 of Section 4.
2. Perform a total of 5 NFEA tensile tests $j = 1…5$ pairwise for integration points I1/I11, I2/I10, I3/I9, I4/I8, and I5/I7, such that one solid element represents the behavior of one integration point of the shell element, as shown in Fig. 8. The residual stress states of the first integration points in pairs are incorporated into the solid element at the bottom (element 1) and the second ones to solid at the top (element 2). Apply the same magnitude of residual stresses to every internal integration point of the solid despite the location of the point. Because of symmetry, the magnitudes of residual stresses in pairs are identical but opposite signs. This causes bending moments

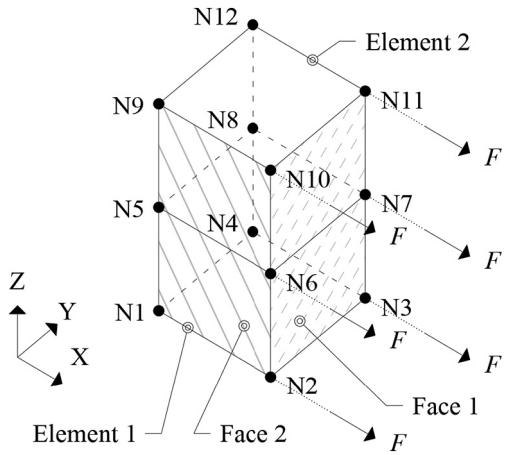

Fig. 7. Nonlinear solid element analysis in Matlab script.

Table 4
Boundary conditions of the Matlab script.

DOF	N1	N2	N3	N4	N5	N6	N7	N8	N9	N10	N11	N12
U_X	0	–	N2	0	0	N2	N2	0	0	N2	N2	0
U_Y	–	N1	0	0	N1	N1	0	0	N1	N1	0	0
U_Z	0	0	0	0	–	–	–	–	–	N9	N9	N9

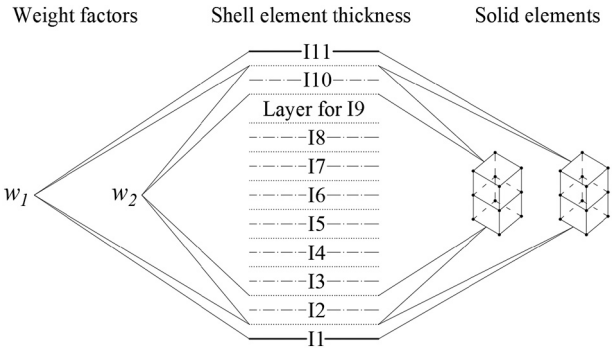

Fig. 8. Solid elements of Matlab script representing the integration points I1-I11 of the shell element.

about X- (σ_{TB}) and Y-axes (σ_{LB}). The applied MPC restraints force the faces to displace in planes such that the residual stress state, i.e. internal moments, will not be released and cause curvature (analogous to the curved tensile coupon in the cutting method).

3. Perform one NFEA tensile test $j = 6$ for integration point I6, having no residual stresses in elements 1 and 2.
4. Combine these 6 separate NFEA tensile tests to a single stress-strain curve by calculating the corresponding total through-thickness stress $\sigma_{Tot,i}$ at strain increment i by:

$$\sigma_{Tot,i} = \sum_{j=1}^{6} w_j \bullet \sigma_{ij} \tag{11}$$

where σ_{ij} is the corresponding stress of analysis j, and w_j is the weight factor of the analysis. Weight factors w_j are the relative influence areas of points I1-I11 in the thickness direction, see Fig. 8. Therefore, w_1 (I1/I11) $= w_6$ (I6) $= 1/10$, and for the remaining analyses $j = 2\ldots5$, $w_j = 1/5$. If strain increments i do not coincide between the analyses j in σ_{ij} (due to force-controlled analysis), linear interpolation can be used in determining the stress values σ_{ij} at identical strain increments before summation in Eq. (11).

Because flat and corner regions have different residual stress magnitudes (Fig. 2) and flat region comprises both the flat and extended corner material, the entire cross-section must be divided into three separate areas A_{MP}, A_{NC} and A_{CC} shown in Fig. 3. A_{MP} has residual stress and material models both according to the flat region. A_{NC} has residual stresses according to the flat region and material model according to the corner region, whereas A_{CC} has residual stress and material models both according to the corner region.

Eq. (11) provides the stress-strain curve over the thickness of the material, but not over the entire cross-section. Therefore, the procedure presented above must be carried out for all areas A_{MP}, A_{NC} and A_{CC}. Then, the total stress-strain curve over the thickness and around the cross-section, i.e., the EMM, is obtained by combining these three stress-strain curves similarly as in Eq. (11). In this case, $j = 1\ldots3$ (A_{MP}, A_{NC}, A_{CC}), weights w_j are the relative portions of areas A_{MP}, A_{NC}, and A_{CC} to the total cross-sectional area, and σ_{ij} are the stresses from the stress-strain curves of A_{MP}, A_{NC}, and A_{CC} over the entire material thickness.

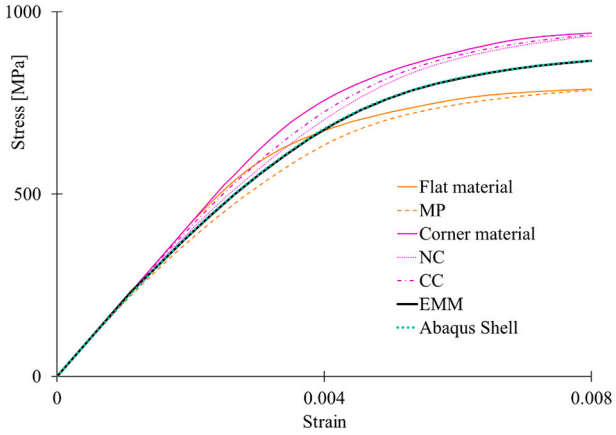

Fig. 9. EMM of the square section 120x120x8 S700. Note that the EMM and Abaqus Shell models are virtually identical, making the continuous solid line for EMM appear dotted.

Fig. 9 illustrates the EMM procedure for the S700 square section 120x120x8 (height $H = 120$ mm, width $W = 120$ mm, and thickness $t = 8$ mm). The base material for the flat region, "Flat material", is plotted in the figure. The curve "MP" follows below Flat material, which accounts for the effects of σ_{LB} and σ_{TB} according to Eqs. (2) and (4) and represents the stress-strain curve over the entire thickness, i.e., the outcome of Eq. (11), for the region A_{MP}. Similarly, the figure presents the base material for the corner region ("Corner material") and reduced stress-strain curves for the regions A_{NC} ("NC") and A_{CC} ("CC"). By combining the curves MP, NC and CC using the relative weights of areas A_{MP}, A_{NC} and A_{CC}, the curve "EMM" is obtained. Eventually, this curve reaches the mean of Flat and Corner material curves, which is expected because both the flat and corner materials constitute about half of the cross-section. Fig. 9 presents also the EMM obtained by using the Abaqus shell element model, where the stress-strain curve is generated by modelling the entire cross-section with shells and tensioning it. The shell element model provides a stress-strain curve that is nearly identical with EMM (within the used figure resolution). Consequently, it can be deduced that the procedure for constructing the EMM is valid.

7. Finite element modelling for buckling analysis

In this study, the EMM is validated on a series of buckling analyses of compression members. The analyses are performed by the Abaqus software [4] for shell and beam element models. Shell models represent "accurate" results, i.e., they are considered as numerical experiments, against which the beam models are compared. In shell models, residual stresses are directly incorporated into the NFEA as initial stresses over the cross-section. For the beam element models, the effects of residual stresses and strength enhancements of corners are incorporated by EMM instead of initial stresses and separate material regions. Consequently, the accuracy of the EMM is validated by comparing the results between the shell and beam element models.

7.1. Shell element models

The element type of S4R with Simpson's integration having 11 integration points through the material thickness is used in shell element models. The geometry of the arc of the corner region has been modelled with four straight faces, i.e., modelling the geometry from NC to CC (Fig. 3) by using one additional point along the arc, at 1/4 of the total arc length. The outer surface corner radius R_o is 2 t, 2.5 t or 3 t in the cases of $t \leq 6$, $6 < t \leq 10$ and $10 < t$ mm, respectively.

The used global coordinate system in all buckling analyses in the shell and beam element models follows the right-hand rule and is presented in Figs. 10 and 12. This system differs from the local residual stress coordinate system used in the Matlab script of Fig. 7, having Z-axis in the direction of the member length. Boundary conditions were modelled by coupling the nodes of the cross-section at the top and bottom ends to boundary nodes using Abaqus "Beam" type MPCs, see Fig. 10. Boundary nodes are located at the distance of 10 mm above and below the member ends and this Z-distance has been considered in the member length L. Horizontal location in X- and Y-directions is modelled according to the load eccentricity of the studied case. Actual boundary conditions, i.e., translational and rotational restrictions, are applied to top and bottom boundary nodes. Geometrical imperfections, i.e., local imperfection e_3, and global sinusoidal half-and full waves e_1 and e_2 were obtained as the lowest applicable modes from the eigenvalue buckling analysis, see Fig. 1. The average mesh size of the models was $W/12$ and $H/12$ to the width (X) and height direction (Y). In the longitudinal Z-axis direction, mesh size was 4 times the minimum of the mesh sizes in the X or Y direction.

The material was modelled according to von Mises yield surface and associated plastic flow with isotropic hardening. The stress-strain curve was determined according to Section 3. It should be noted that the measured engineering stresses and strains presented in Table 1 were not converted to true stresses and strains in the shell model because of the comparison of the results between shell and beam models. This has a slightly conservative effect on the capacity and is considered to account for somewhat limited knowledge about the strain rate effect presented in Section 3. Residual stresses were modelled as initial stresses, and corresponding equivalent plastic strains by the Abaqus Fortran subroutines SIGINI and HARDINI. Initial stresses were incorporated directly into the integration points of the shell element according to the model in Fig. 2.

Residual stresses were applied to the calculation models in a preliminary static analysis step using Newton's method. In some analyses, an additional subsequent static analysis step using Newton's method was applied to incorporate the possible initial forces into the model. The actual buckling analysis was performed by the arc-length method. Displacement-controlled compressing load in Z-direction was used in every buckling case except in sway columns, in which the force control was used.

Shell models must give realistic results because they are treated as numerical experiments. Therefore, shell models were validated against 30 experimental buckling tests carried out by Ma et al. [28] and Somodi and Kövesdi [33]. The experiments consist of a variety of cold-formed rectangular and square sections of grade S700 steel members, considering both centrically compressed columns and beam-columns. Residual stresses have been incorporated into the validation models according to Eqs. (2)–(4) by considering 70% of the σ_{LB} (Section 5) and 100% of σ_{TB}. Close correspondence is obtained between experimental tests and shell models as shown in Fig. 11. The ratio of the experimental test capacities divided by the shell model capacities has a mean of 1.016 and the coefficient of variation (COV) of 0.05. These statistics have been adopted for modelling uncertainty in Monte Carlo-simulations presented in Section 9.

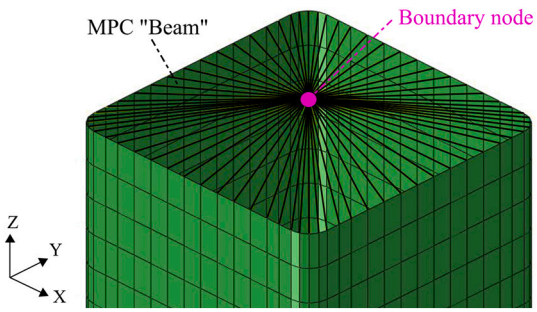

Fig. 10. MPCs at the top end of the member.

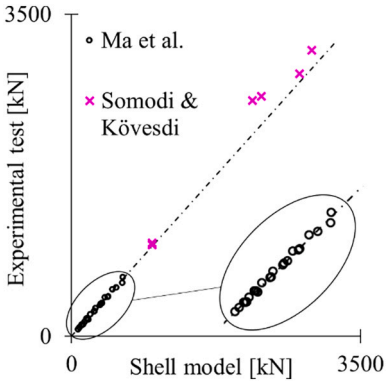

Fig. 11. Global buckling capacities in the shell model validation.

7.2. Beam element models

Abaqus beam element B31 is used in beam models. The cross-section is modelled using Abaqus "ARBITRARY" definition, which enables the modelling of rounded corners. Stress-strain curve of the material is the EMM, hence residual stresses have not been incorporated explicitly. The mesh size (element length) varied from 80 to 250 mm depending on the case, and local imperfection e_3 (see Fig. 1) has been neglected. The other features in beam models are identical to shell models presented in Section 7.1.

8. Parametric studies

Parametric studies are carried out to illustrate the shortcoming of the EGI approach and to provide an overall view of the capabilities of the EMM. Fig. 12 presents three isolated columns, IC1-IC3, which are used throughout the parametric studies and Monte Carlo-simulations to investigate columns under various support and loading conditions. Isolated column IC1 is a pinned column. The force N_d compresses the column while the uniform bending moment M_d (given as percentage of the design bending resistance according to Eurocode 3) acts along the length of the member. IC2 has all translational and rotational DOFs zero, i.e. fixed support, at the bottom end A. At the top end B, X- and Y-

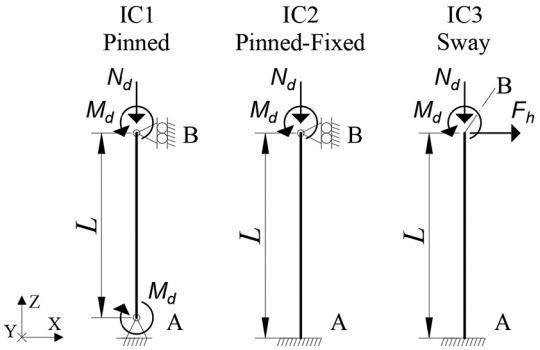

Fig. 12. Boundary conditions and applied loads of isolated columns IC1-IC3.

translations are restrained. In IC2, the moment M_d causes varying bending moment along the length of the member. IC3 is a sway column having a fixed support at bottom end A. Additionally, IC3 has a horizontal force F_h that represents the equivalent horizontal force of the geometrical sway imperfection and possible wind load. In planar 2D studies, rotational DOF about X-axis and translational DOF in Y-direction have been additionally restrained in boundary nodes such that buckling occurs in the XZ-plane.

Material parameters are according to the mean values of Tables 1 and 3 and residual stresses according to Eqs. (2)–(4) considering 70% of σ_{LB}. The EGI approach can not consider multiple material models in a beam cross-section. Therefore, in the parametric study of Section 8.1, the entire cross-section is exceptionally modelled by the material model and residual stresses of the flat region. In all other analyses, including Monte Carlo-simulations of Section 9, the separate material and residual stress properties have been considered for the corner, near corner, and flat regions, as discussed in Sections 2–6.

8.1. Shortcomings of equivalent geometrical imperfections

To emphasize the need for the new EMM method, shortcomings of the EGI (see Section 1) are illustrated by comparing the column buckling capacities of the shell model (M_{Shell}) to beam models with EMM (M_{EMM}) and EGI (M_{EGI}). Consider a planar CFRHS column of size 140x140x8, which is pinned (IC1) and the point moment $M_d = 0$. M_{Shell} and M_{EMM} have a single geometrical bow imperfection $e_1 = L/1000$. The magnitude $L/1000$ is widely adopted to nominal models in ADMs, and it covers, to some extent, both the effects of geometrical imperfections and load eccentricities [38]. The bow imperfection e_1 for M_{EGI} has been determined similarly as in [9], i.e., by trial and error, such that columns with lengths of $L = 4$ m have identical capacities between M_{Shell} and M_{EGI}. This EGI magnitude was found to be $e_1 = L/400$. It is worth highlighting that the only difference between M_{EMM} and M_{EGI} is that, whereas M_{EMM} has the EMM and bow $e_1 = L/1000$, M_{EGI} has the same material model with M_{Shell} and bow $e_1 = L/400$.

Fig. 13 presents load-displacement curves for the prescribed models with varying buckling lengths $L = 1$, 2, 3, 4, 5, 6, 7, and 8 m (non-dimensional slenderness of EN 1993-1-1, $\bar{\lambda}$≈0.4–2.9 [1]). M_{EGI} follows M_{Shell} well in the case of $L = 4$ m because the bow magnitude $L/400$ was determined based on that specific column. However, if the slenderness decreases, e.g., $L = 1$ m, M_{EGI} is too stiff and underestimates the maximum capacity by about 4.1%. In the case of higher slenderness (e.g., $L = 8$ m), M_{EGI} behaves too flexibly. Stiffness of structural members must be realistically modelled such that forces will be correctly redistributed in the nonlinear analysis. M_{EMM} fulfils this property, providing a close agreement with M_{Shell} in the stiffness and maximum capacity.

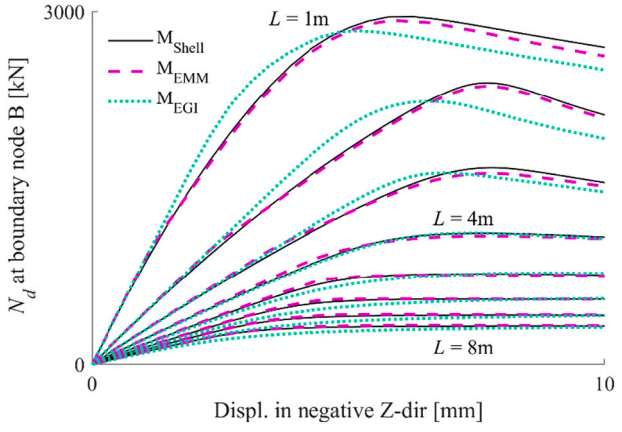

Fig. 13. Load-displacement curves of Shell, EMM and EGI models for case IC1 with cross-section 140x140x8.

The differences between M_{Shell} and M_{EGI} become even more evident when considering varying cross-section sizes and boundary conditions: For a column IC1 with $M_d = 0$, rectangular cross-section 160x80x8 with $\bar{\lambda}$≈0.7 (L = 2 m), M_{EGI} with the bow e_1 = L/400 underestimates the buckling capacity by 6.4% in the major axis buckling direction. If the same column buckles in the minor axis direction with a slenderness of $\bar{\lambda}$≈2.1 (L = 3.45 m) having a constant initial bending moment M_d = 5% of the design bending resistance, M_{EGI} overestimates the buckling capacity by 4.2%. If M_d is increased to 20% and 40%, M_{EGI} overestimates the capacity by 7.9% and 9.8%, respectively. For the same columns, M_{EMM} has a maximum underestimation of 1.1% and an overestimation of 0.6%.

Additional challenges are faced in the case of sway column (IC3) that is rigidly fixed to the foundation and resist horizontal loads. Sway column probably collapses due to the plastic hinge near the foundation, thus the bow imperfection e_1 has a minor influence on the capacity. However, residual stresses affect the formation of the plastic hinge, and hence the second-order effects in a column. Therefore, sway columns would need a separate shape and magnitude of EGI which further complicates the design task. In EMM approach, the effects of residual stresses are automatically considered also in the plastic hinge near foundation.

The results above illustrate how the sensitivity of the structure to geometrical imperfections determines whether the effects of residual stresses are over- or underestimated in the EGI approach. This inaccuracy drives the need for a more accurate approximation method because the inaccuracy must be considered in the safety factors thus affecting the efficiency of the ADM.

8.2. Pinned columns

Table 5 presents the parametric studies of pinned columns. Case P1 considers 6 planar (2D) analyses for a square cross-section 250x250x10, having a fixed length L = 6.1 m for every analysis such that the non-dimensional slenderness $\bar{\lambda}$=1.2. The bending moment M_d is varied between 0% and 40% of the bending resistance of the cross-section as determined by EN 1993-1-1. The maximum capacities obtained by M_{Shell} and M_{EMM} are compared in terms of M_{EMM}/M_{Shell}. The table presents the mean, COV, and the minimum (Min) and the maximum (Max) differences in percentages. In case P1, the mean is 98%, hence M_{EMM} yields 2% lower capacity than M_{Shell} on average. The small COV (0.18%) indicates that the bending moment does not affect the approximation accuracy of the EMM significantly. Fig. 14 presents the load-displacement curves of case P1, and close correspondence between M_{EMM} and M_{Shell} is obtained also in stiffness. It should be noted that in the following figures, the initial bending moment M_d causes initial Z-displacements, hence displacements in the following figures do not start from the origin if M_d is present.

Cases P1-P6 explore 2D square sections with varying width-to-thickness ratios, non-dimensional slenderness and bending moments. The accuracy of EMM is good throughout the entire range of parameters. Cases P2 and P3 indicate that a huge bending moment, which is 50% in case P3, decreases the mean by only about 1% when compared to the small bending moment (5%) of case P2. It was also observed that the EMM yields slightly more conservative results in the intermediate slenderness level ($\bar{\lambda}$ = 1–1.4) than in low or high slenderness.

Cases P7-P14 study 2D rectangular sections with varying width-to-height ratios. Cases with major axis bending (cases P7, P9, P11, P13) yield the lowest mean values, i.e. the highest conservativeness of the EMM approach. The conservativeness increases probably because corner and near-corner regions, which have more beneficial material models and residual stress levels compared to the flat region, have longer lever arms to the center of gravity in the major axis direction. M_{Shell} accounts for these lever arms providing additional stiffness to the cross-section, whereas M_{EMM} has a smaller lever arm because of the averaged

Table 5
Results of the parametric study for pinned columns (IC1).

Case	Cross-sect.	Buckling Axis	L [m] and M_d [%]		$\bar{\lambda}$	Capacity M_{EMM} / M_{Shell} [%]			
			Fixed	Variable		Mean	COV	Min	Max
P1	250x250x10	–	L: 6.1	M_d: 0.0, 2.5, 5.0, 10.0, 20.0, 40.0	1.2	98.0	0.18	97.7	98.2
P2	150x150x10	–	M_d: 5.0	L: 1.0, 2.0, 3.0, 4.0, 5.0, 6.0, 7.0, 8.0	0.3… 2.7	98.4	0.67	97.2	99.3
P3	150x150x10	–	M_d: 50.0	L: 1.0, 2.0, 3.0, 4.0, 5.0, 6.0, 7.0, 8.0	0.3… 2.7	97.4	0.40	96.8	97.8
P4	150x150x5	–	M_d: 5.0	L: 1.0, 2.0, 3.0, 4.0, 5.0, 6.0, 7.0, 8.0	0.3… 2.6	99.2	1.03	98.3	101.7
P5	100x100x8	–	M_d: 0.0	L: 1.0, 1.5, 2.0, 2.5, 3.0, 3.5, 4.0, 4.5, 5.0, 5.5, 6.0	0.5… 3.1	98.8	1.12	97.2	100.6
P6	60x60x3	–	M_d: 0.0	L: 0.4, 0.8, 1.2, 1.6, 2.0, 2.4, 2.8, 3.20, 3.6, 4.0	0.3… 3.3	99.0	0.76	97.9	100.2
P7	250x100x10	Major	L: 5.3	M_d: 0.0, 2.5, 5.0, 10.0, 20.0, 40.0	1.2	95.1	1.27	92.6	96.1
P8	250x100x10	Minor	L: 2.6	M_d: 0.0, 2.5, 5.0, 10.0, 20.0, 40.0	1.2	99.8	1.14	98.9	102.2
P9	250x100x10	Major	M_d: 10.0	L: 2.0, 4.0, 6.0, 8.0, 10.0, 12.0	0.5… 2.7	96.0	0.63	95.6	97.4
P10	250x100x10	Minor	M_d: 10.0	L: 1.0, 2.0, 3.0, 4.0, 5.0, 6.0	0.5… 2.8	100.1	0.90	98.6	101.1
P11	200x100x10	Major	L: 4.3	M_d: 0.0, 2.5, 5.0, 10.0, 20.0, 40.0	1.2	95.3	0.92	93.5	96.0
P12	200x100x10	Minor	L: 2.5	M_d: 0.0, 2.5, 5.0, 10.0, 20.0, 40.0	1.2	99.2	1.10	97.9	101.2
P13	150x100x8	Major	M_d: 10.0	L: 2.0, 3.0, 4.0, 5.0, 6.0, 7.0, 8.0	0.7… 2.8	97.3	0.36	96.8	97.7
P14	150x100x8	Minor	M_d: 10.0	L: 1.4, 2.0, 2.6, 3.2, 3.8, 4.4, 5.0	0.7… 2.4	99.2	0.60	98.3	99.9
P15	200x200x10	Double	M_d: 0.0	L: 2.0, 2.5, 3.0, 3.5, 4.0, 4.5 5.0, 5.5, 6.0, 6.5, 7.0, 7.5, 8.0, 8.5, 9.0, 9.5, 10.0, 10.5 11.0, 11.5, 12.0	0.5… 3.0	98.6	0.42	98.0	99.4
P16	100x50x4	Double	$M_{d,min}$: 2.5 $M_{d,maj}$: 25.0	L: 0.5, 1.0, 1.5, 2.0, 2.5, 3.0, 3.5, 4.0	0.3… 2.2	99.4	0.28	98.8	99.8

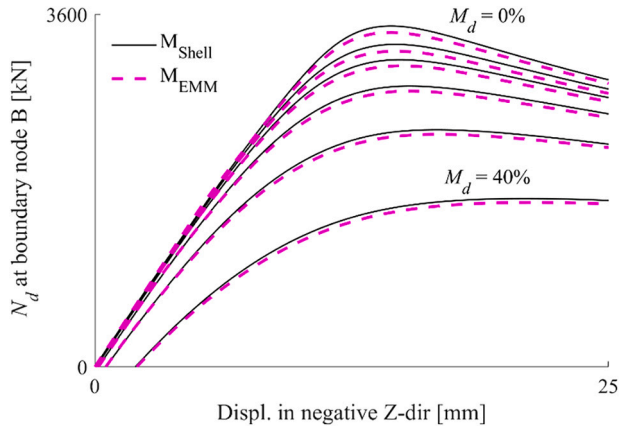

Fig. 14. Load-displacement curves of the case P1, Pinned 250x250x10.

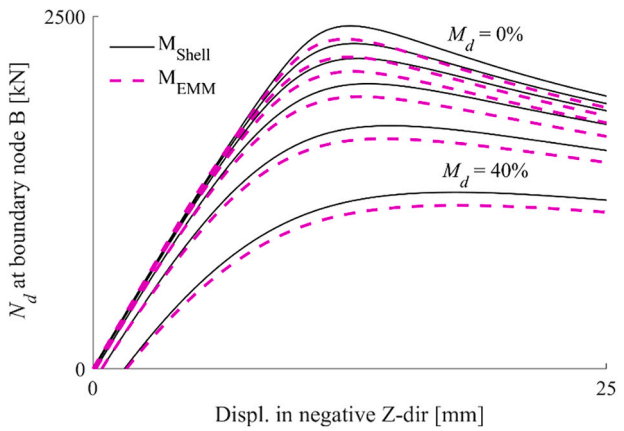

Fig. 15. Load-displacement curves of the case P7, Pinned major axis 250x100x10.

material model for the entire cross-section. On the other hand, M_{EMM} can also have a longer lever arm than M_{Shell} in minor axis bending (cases P8, P10, P12, P14), such that EMM provides even higher capacities than M_{Shell} as shown in the Max values. Fortunately, these overestimated capacities are rather minor, and the mean values are close to 100%. Fig. 15 presents load-displacement curves for case P7, which has the lowest mean of the pinned cases, 95.1%. When the same cross-section with the same slenderness buckles in the minor axis direction (case P8), the load-displacement curves shown in Fig. 16 are obtained. Despite the slight capacity differences, the EMM approach results in acceptable level of accuracy also for rectangular sections.

Cases P15-P16 consider 3D columns in double-axis buckling. In these models, the bow imperfection $L/1000$ is in the intermediate axis direction, i.e. along the diagonal between X- and Y-axes. Case P15 considers no bending moment, whereas case P16 has 2.5% M_d in the minor axis and 25% M_d in the major axis direction. In these cases, the EMM is in very good agreement with the shell model. This is expected because only 2 of the 4 corners have long lever arms and the other 2 corners locate (square) or almost locate (rectangular) in the axis that passes through the center of the gravity, thus averaging out the lever arm effect.

8.3. Pinned-fixed and sway columns

Table 6 presents the results of pinned-fixed columns. Cases P17-P20 yield similar results as in the case of pinned columns. A comparison of pinned cases P13 and P14 to cases P19 and P20 indicate that IC2 boundary conditions almost double the COV (0.36%–0.60% to 1.17%–1.29%). However, COV is still relatively low and the EMM approach is sufficiently accurate for practical purposes.

Table 7 presents the results for sway columns. In these cases, the vertical force F_h is expressed in terms of percentages of the compressive force N_d. Therefore, F_h is not constant, and it is increasing during the analysis with N_d. In cases P21-P23, F_h has the basic value of the sway imperfection, 0.5%, i.e. 1/200, according to Eurocode 3. In cases P24-P25, F_h is in the negative X-axis direction and equals N_d. Results of sway columns are similar to results of pinned and pinned-fixed columns.

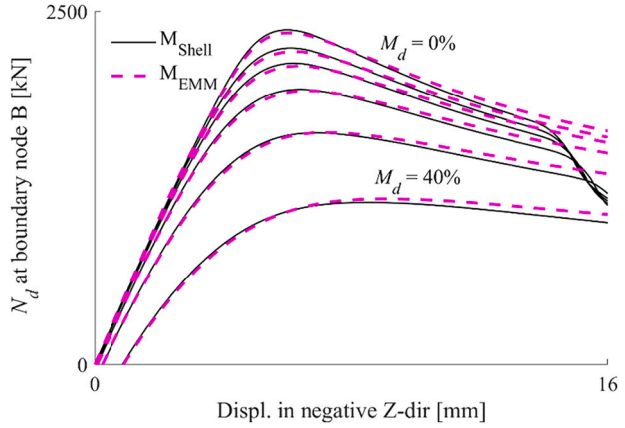

Fig. 16. Load-displacement curves of the case P8, Pinned minor axis 250x100x10.

8.4. Cross-section class 4 structures and pure bending

Beam elements are not capable of accounting for local stability issues within the cross-section. Therefore, sections are classified into cross-section classes (CL) which have varying requirements: CL2 sections cannot form plastic hinges, CL3 sections cannot achieve plastic bending resistance, and the effective cross-section must be considered with CL4 sections [1]. Load-displacement curves of minor axis buckling were shown in Fig. 16 for cross-section 250x100x10 (case P8), in which the 250 mm wide side belongs to CL2 in uniform compression. The figure shows how the capacities of M_{Shell} suddenly drop near the end of the curves, whereas M_{EMM} does not recognize this behavior. This kind of local stability issue can be considered in beam element-based ADM by using strain limits based on the continuous strength method [39], [40]. However, using strain limits requires that the beam model accurately replicates the behavior of the real structure such that monitored strains in the analysis are correct. Table 8 presents results for the rectangular section 400x200x10 which has CL4 webs in uniform compression. Cases P26 and P27 do not consider low slenderness values ($0.8 \leq \bar{\lambda}$) and CL4 webs are not entirely in compression (they are subject to bending), hence the accuracy of the EMM is rather good. For minor axis buckling (case P28), however, CL4 webs are entirely compressed, and a wider range of slenderness is covered. Consequently, M_{EMM} yields about 4% higher capacities on average and about 21% higher capacity at maximum. Load-displacement curves of this case are shown in Fig. 17. The figure shows how the capacity of M_{Shell} suddenly drops in the case of shorter columns $L = 2$, 4 and 6 m. Naturally, M_{EMM} does not recognize this local phenomenon, but it follows excellently M_{Shell} up to failure. This indicates that the EMM approach is suitable for every cross-section class, if proper strain limits to account for local buckling are developed, for example, by the continuous strength method.

In addition to buckling phenomena, the EMM approach must also be suitable for beams that resist pure bending moments. Fig. 18 presents the moment-displacement curves for various cross-sections in planar analysis. These cases are IC1 columns, in which M_d is increased while $N_d = 0$. M_{EMM} follows well M_{Shell}, i.e. the EMM approach is applicable for the pure bending situation also. It should be noted that CFRHS are not prone to lateral-torsional buckling, hence that phenomenon has not been examined.

9. Accuracy of EMM in Monte Carlo-simulations

Practical utilization of ADMs requires safety factors which can be developed by the reliability studies. Monte Carlo-simulations are commonly used in these studies in conjunction with NFEA [15], [16]. Monte Carlo-technique may need thousands of nonlinear analyses such that beam elements are preferred. The parametric study of Section 8 did not consider varying material properties, residual stress magnitudes and bow imperfections, whereas in reliability studies, these parameters are

Table 6
Results of the parametric study for pinned-fixed columns (IC2).

Case	Cross-sect.	Buckling Axis	L [m] and M_d [%]		$\bar{\lambda}$	Capacity M_{EMM} / M_{Shell} [%]			
			Fixed	Variable		Mean	COV	Min	Max
P17	140x140x8	–	M_d: 5.0	L: 1.0, 1.5, 2.0, 2.5, 3.0, 3.5, 4.0, 4.5, 5.0, 5.5, 6.0, 6.5, 7.0, 7.5, 8.0, 8.5, 9.0, 9.5, 10.0	0.3… 2.5	98.3	0.43	97.6	99.0
P18	140x140x8	–	L: 4.0	M_d: 0.0, 2.5, 5.0, 10.0, 20.0, 40.0	1.0	97.7	0.18	97.5	97.9
P19	150x100x8	Major	M_d: 10.0	L: 2.0, 3.5, 5.0, 6.5, 8.0, 9.5, 11.0	0.5… 2.7	97.8	1.29	95.5	99.4
P20	150x100x8	Minor	M_d: 10.0	L: 1.5, 3.0, 4.5, 6.0, 7.5, 9.0	0.5… 3.1	99.4	1.17	98.1	101.1

Table 7
Results of the parametric study for sway columns (IC3).

Case	Cross-sect.	Buckling Axis	F_h [%]	L [m], and M_d [%]		$\bar{\lambda}$	Capacity M_{EMM} / M_{Shell} [%]			
				Fixed	Variable		Mean	COV	Min	Max
P21	80x80x4	–	0.5	M_d: 0.0	L: 0.5, 0.75, 1.0, 1.25, 1.5, 1.75, 2.0, 2.25, 2.5	0.6… 3.1	98.7	0.62	97.7	99.6
P22	200x100x10	Major	0.5	M_d: 0.0	L: 0.5, 1.0, 1.5, 2.0, 2.5, 3.0, 3.5, 4.0, 4.5, 5.0	0.3… 2.8	97.3	1.02	95.6	98.7
P23	200x100x10	Minor	0.5	M_d: 0.0	L: 0.5, 1.0, 1.5, 2.0, 2.5, 3.0, 3.5, 4.0, 4.5, 5.0	0.5… 4.8	100.3	1.48	98.2	102.2
P24	200x100x10	Major	−100.0	M_d: 2.5	L: 0.5, 1.0, 1.5, 2.0, 2.5, 3.0, 3.5, 4.0, 4.5, 5.0	0.3… 2.8	96.4	0.39	95.7	97.2
P25	200x100x10	Minor	−100.0	M_d: 2.5	L: 0.5, 1.0, 1.5, 2.0, 2.5, 3.0, 3.5, 4.0, 4.5, 5.0	0.5… 4.8	100.8	1.27	98.3	102.1

Table 8
Results of the parametric study for pinned columns (IC1), CL 4.

Case	Cross-sect.	Buckling Axis	L [m] and M_d [%]		$\bar{\lambda}$	Capacity M_{EMM} / M_{Shell} [%]			
			Fixed	Variable		Mean	COV	Min	Max
P26	400x200x10	Major	M_d: 0.0	L: 7.0, 10.0, 13.0, 16.0, 19.0	0.9… 2.5	98.3	0.70	97.4	99.3
P27	400x200x10	Major	M_d: 30.0	L: 6.0, 9.0, 12.0, 15.0, 18.0	0.8… 2.4	96.5	0.19	96.3	96.9
P28	400x200x10	Minor	M_d: 0.0	L: 2.0, 4.0, 6.0, 8.0, 10.0, 12.0	0.5… 2.7	103.9	7.57	99.1	121.3

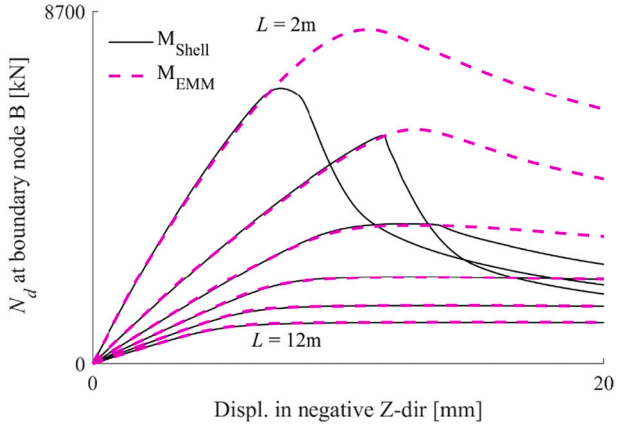

Fig. 17. Load-displacement curves of the case P28, Pinned minor axis 400x200x10, CL4.

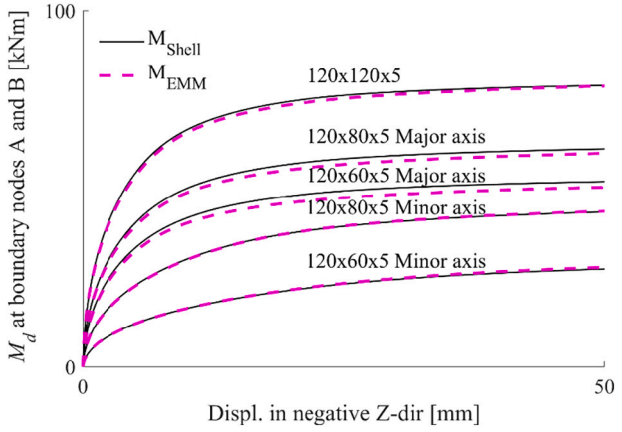

Fig. 18. Load-displacement curves in the case of pure bending.

random variables. Therefore, with a similar comparison as in the parametric study, the accuracy of the EMM is determined in this Section for reliability applications by carrying out Monte Carlo-simulations.

The EMM does not affect loads, hence only the random variables contributing to the resistance are considered in simulations. Statistical properties for the flat and corner materials were given in Tables 1–3. C_{fy} has been truncated based on measured lower and upper bound values, into the interval [1.06, 1.34], to prevent unrealistically high C_{fy} factors. The remaining random variables are shown in Table 9. Properties of width, height and local imperfection were determined based on 150 measurements and thickness based on 271 measurements obtained from the manufacturer. The maximum out-of-plumb, i.e. the combined effect of e_1 and e_2, was determined based on 127 measurements conducted for over 500 mm long specimens in studies [41], [42], [28]. The actual magnitudes of e_1 and e_2 were determined based on a ratio that the contribution of e_2 is about 30% of e_1 [41], [15].

The authors have not found any measurements for load eccentricity. The draft prEN 1993-1-1 [24] suggests assuming the mean values as nominal values, and standard deviations taken as half of the interval between the nominal and the lower bound values of the applicable tolerance interval in EN 1090–2 [43] in the case of unspecified variables. Therefore, load eccentricities at the top and bottom have been assumed uncorrelated with the means of 0 and standard deviations of 2.5 mm. Additionally, load eccentricity is truncated to the allowed tolerance interval [−5 mm, +5 mm].

Statistical properties of residual stresses are based on [7], and the sampled values of $\sigma_{LB,Flat}$ and $\sigma_{LB,Corner}$ have been multiplied by 0.7 according to Section 5. This procedure also reduces the scatter of these components. However, this is justified since COV of $\sigma_{0.05}$ is almost twice the COV of f_y (see Table 1), hence the reduced scatter has probably been included in the variation of $\sigma_{0.05}$. Correlations were found between some of the variables and their correlation coefficients are presented in Tables 10 and 11. Latin hypercube sampling is employed in simulations, and according to preliminary tests, 250 samples were sufficient per each simulation to obtain realistic estimate for statistical distribution of the resistance.

Tables 12 and 13 present altogether 14 Monte-Carlo simulations, R1-R14, that were carried out in this study. The simulations cover a wide range of non-dimensional slenderness from 0.4 to 2.8, various cross-section sizes, and a wide range of width-to-thickness ratios of the cross-section from 10 to 25. Simulations R1-R10 are for pinned columns (IC1) without end moment M_d, whereas simulations R11-R14 are special cases of R1, R6 and R7 such as double-axis buckling or pinned-fixed column.

Obtained capacities M_{EMM} and M_{Shell} are compared in Tables 12 and 13. High accuracy is achieved by the EMM even though material and geometrical properties vary between analyses. On average, the capacity of M_{EMM} is about 98% of M_{Shell}, and the COV of the difference only about 1%. Tables 12 and 13 present also the percentage difference for the sample standard deviations s_{EMM} and s_{Shell}. These relative differences are remarkably higher than differences in capacity because the same absolute error causes a significantly higher relative difference to a small standard deviation than to the total capacity. Sample standard deviations differ by up to 13%, which is still a fairly accurate representation for reliability studies. It is also worth noting that the particular element formulations of beam and shell elements cause unavoidable differences in results. Therefore, the error is not entirely due to the EMM. Based on the above, the EMM approach is valid also for Monte Carlo-simulations in reliability studies.

Table 9
Random variables for member resistance.

Property	Description	Distribution	Parameters	Ref.
W	Width	Normal	$\mu = 1.00$, $\sigma = 3.17$e-3 [$1/W$]	DSet
H	Height	Normal	$\mu = 1.00$, $\sigma = 3.17$e-3 [$1/H$]	DSet
t	Thickness	GEV	$\mu = 0.9824$, $\sigma = 1.24$e-2, $\xi = 4.60$e-2 [$1/t$]	DSet
e_1	1. bow imperfection	Normal	$\mu = 0.0$, $\sigma = 2.163$e-4 [$1/L$]	[28, 41, 42, 15]
e_2	2. bow imperfection	Normal	$\mu = 0.0$, $\sigma = 6.489$e-5 [$1/L$]	[28, 41, 42, 15]
e_3	Local imperfection	Normal	$\mu = 3.56$e-4, $\sigma = 2.20$e-3 [max($1/W$;$1/H$)]	DSet
e_{top}	Load eccentricity at top	Normal	$\mu = 0.0$, $\sigma = 2.5$ [mm]	[24, 43]
e_{bot}	Load eccentricity at bottom	Normal	$\mu = 0.0$, $\sigma = 2.5$ [mm]	[24, 43]
$\sigma_{LB,Flat}$	Longit. res.str. in flat	Normal	$\mu =$ Eq. (2), $\sigma = 0.206$ [$1/f_y$]	[7]
$\sigma_{LB,Corner}$	Longit. res.str. in corner	Normal	$\mu =$ Eq. (3), $\sigma = 0.196$ [$1/f_y$]	[7]
$\sigma_{TB,Flat}$	Trans. r. s. in flat and corner	Normal	$\mu =$ Eq. (4), $\sigma = 0.155$ [$1/f_y$]	[7]
θ_R	Modelling uncertainty in resistance	Normal	$\mu = 1.016$, $\sigma = 0.0508$	[15]

Table 10
Correlation coefficients for material parameters [DSet].

	f_y	f_u	$\sigma_{0.05}$
f_y	1.0	0.70	0.70
f_u	symm.	1.0	0.0
$\sigma_{0.05}$	symm.	symm.	1.0

Table 11
Correlation coefficients for residual stress components [7].

	$\sigma_{LB,Flat}$	$\sigma_{LB,Corner}$	$\sigma_{TB,Flat}$
$\sigma_{LB,Flat}$	1.0	0.80	0.76
$\sigma_{LB,Corner}$	symm.	1.0	0.69
$\sigma_{TB,Flat}$	symm.	symm.	1.0

10. Conclusions

The effective material model (EMM) proposed in this study replicates the stress-strain curve that would be obtained by conducting the tensile test for the entire cold-formed cross-section. Consequently, the effects of residual stresses and corner strength enhancements are included in the EMM such that their consideration in advanced design method is effortless.

The accuracy of the EMM was validated by comparing the buckling capacities of beam element-based EMM models with shell element models in which the residual stresses and corner strength enhancements were explicitly modelled. Validation was carried out by performing over 3700 numerical buckling tests for a wide range of various cross-section sizes, boundary conditions, and material and geometrical properties. Excellent accuracy was achieved by the EMM approach (excluding very slender cross-sections (CL4) where local buckling governs the load-bearing capacity): On average, EMM capacities were about 98% of the shell model capacity, the minimum difference being 93% and a maximum of 105%. On average, the coefficient of variation for the capacity differences was under 1%, hence the minimum and maximum differences occurred only in some rare analyses. Additionally, Monte Carlo-simulations were carried out to ensure the applicability of the EMM for reliability studies. The accuracy was deemed sufficient also in these applications, standard deviations differing under 2% on average and 13% at maximum.

Beam elements are not capable of modelling local buckling that can occur in slender sections. This was illustrated in the paper by utilizing EMM approach for a member with cold-formed hollow section 400x200x10 (susceptible to local buckling). In this case, the EMM approach did not detect local buckling and consequently overestimated the capacity. However, the load-displacement curves of the EMM approach traced accurately the curves obtained by shell element models up to the local buckling failure. Therefore, the EMM approach seems applicable also for very slender sections if the allowed strain limits accounting for local buckling have been determined for these sections, e.g. by the continuous strength method.

Through the EMM approach, the material model becomes cross-section specific in addition to steel grade. To be used in a practical design software, the nominal EMM should be generated for each available cross-section and steel grade. This work has to be done only once, and consequently design by the EMM approach is as effortless as with other advanced design methods that use nonlinear material models. Ideally, the EMMs are implemented in the design software in advance such that they are readily available for practitioners using advanced analysis.

Considerable uncertainty exists in corner strength enhancement factors, which were based on only 12 measured values. Therefore, more experimental research is needed in measuring the material properties around the cross-section perimeter. Although tensile tests for entire cross-sections are more laborious than coupon tests, the real EMMs could be accurately formulated based on measurements of the entire section. Consequently, in addition to harmful residual stresses, the beneficial effects of strain hardened cold-formed material could be utilized.

In this study, the EMM was validated for cold-formed rectangular hollow sections made of steel grade S700. The approach is applicable for other steel grades, and perhaps for other types of steel sections also. Hence, additional validation studies for various applications are needed to reveal the full potential of the EMM.

Table 12
Monte Carlo simulations and the accuracy of the EMM for pinned columns.

Case	Cross-section	Buckling Axis	$\bar{\lambda}$	Capacity M_{EMM} / M_{Shell} [%]				s_{EMM}/s_{Shell} [%]
				Mean	COV	Min	Max	
R1	70x70x4	–	1.1	98.1	0.58	95.3	100.2	97.7
R2	50x50x3	–	2.4	99.6	1.55	94.4	104.2	109.1
R3	120x120x5	–	0.7	99.2	0.83	98.0	104.9	99.3
R4	100x100x8	–	0.4	98.7	0.55	96.1	103.8	100.1
R5	40x40x3	–	0.9	97.9	0.46	96.7	100.4	97.4
R6	250x100x10	Major	1.0	96.7	1.16	93.4	100.6	91.3
R7	180x180x10	–	1.3	98.1	1.20	94.9	103.9	103.4
R8	80x40x4	Major	1.6	97.4	1.38	93.7	101.8	103.0
R9	250x250x10	–	2.0	99.7	1.92	95.6	105.2	112.8
R10	160x160x8	–	2.8	100.5	1.83	94.7	105.3	110.6
Average				98.6	1.15	95.3	103.0	102.5

Table 13
Monte Carlo simulations and the accuracy of the EMM for special cases.

Case	Cross-sect.	Description	Capacity M_{EMM} / M_{Shell} [%]				s_{EMM} / s_{Shell} [%]
			Mean	COV	Min	Max	
R11	180x180x10	Double axis buckling for case R7 (IC1)	98.2	0.84	95.5	103.9	100.7
R12	250x100x10	Minor axis buckling for the profile of the case R6 maintaining the same slenderness (IC1)	99.2	0.95	96.1	103.9	100.7
R13	70x70x4	Buckling for case R1 with end moment $M_d = 10\%$ (IC1)	97.9	0.64	95.4	100.3	97.6
R14	180x180x10	Pinned-Fixed for case R7 (IC2)	98.2	0.47	96.1	100.4	97.3
Average			98.4	0.73	95.8	102.1	99.1

CRediT authorship contribution statement

Lauri Jaamala: Conceptualization, Methodology, Software, Formal analysis, Investigation, Writing – original draft, Visualization. **Kristo Mela:** Resources, Writing – original draft, Validation, Supervision, Project administration, Funding acquisition. **Juha Tulonen:** Data curation, Writing – review & editing. **Anssi Hyvärinen:** Data curation, Writing – review & editing.

Declaration of Competing Interest

The authors declare that they have no known competing financial interests or personal relationships that could have appeared to influence the work reported in this paper.

Data availability

The data that has been used is confidential.

Acknowledgements

This research was funded by the Doctoral School of Industry Innovations at Tampere University and SSAB. Computational resources were provided by CSC – IT Center for Science, Finland. The funding and support are gratefully acknowledged.

Appendix A. Supplementary data

The EMMs generated in this study for the profiles presented in Tables 5–8 are provided as Abaqus material cards in supplementary ASCII files.

References

[1] European standard, Eurocode 3 Design of Steel Structures-Part 1.1 General Rules and Rules for Buildings, 2005.
[2] 1993-1-5 EN, Eurocode 3 - Design of Steel Structures - Part 1–5: Plated Structural Elements, 2006.
[3] 4600:2018, A. Australian/ New Zealand Standard, Cold-Formed Steel Structures, 2018.
[4] Abaqus 3DExperience R2019x, Dassault Systemes, 2019.
[5] L. Gardner, N. Saari, F. Wang, Comparative experimental study of hot-rolled and cold-formed rectangular hollow sections, Thin-Walled Structures 48 (2010) 495–507, https://doi.org/10.1016/j.tws.2010.02.003.
[6] J.-L. Ma, T.-M. Chan, B. Young, Material properties and residual stresses of cold-formed high strength steel hollow sections, J Constr Steel Res 109 (2015) 152–165, https://doi.org/10.1016/j.jcsr.2015.02.006.
[7] L. Jaamala, K. Mela, J. Laurila, M. Rinne, P. Peura, Probabilistic modelling of residual stresses in cold-formed rectangular hollow sections, J Constr Steel Res 189 (2022), 107108, https://doi.org/10.1016/j.jcsr.2021.107108.
[8] J. Jönsson, T.-C. Stan, European column buckling curves and finite element modelling including high strength steels, J Constr Steel Res 128 (2017) 136–151, https://doi.org/10.1016/j.jcsr.2016.08.013.
[9] F. Walport, L. Gardner, D.A. Nethercot, Equivalent bow imperfections for use in design by second order inelastic analysis, Structures (Oxford) 26 (2020) 670–685, https://doi.org/10.1016/j.istruc.2020.03.065.
[10] Johnston B. Battermann, G. RH., Behavior and maximum strength of metal columns, ASCE J Struct Div 93 (ST2) (1967) 205–230.
[11] R. Bjoerhovde, Deterministic and Probabilistic Approaches to the Strength of Steel Columns, ProQuest Dissertations Publishing, 1972.
[12] R.D. Ziemian, Guide to stability design criteria for metal structures, 6th ed., John Wiley & Sons, Hoboken, N.J, 2010.
[13] H. Blum, Reliability-Based Design of Truss Structures By Advanced Analysis. Research Report R936, School of Civil Engineering, The University of Sydney, 2013.
[14] W. Liu, K.J.R. Rasmussen, H. Zhang, Modelling and probabilistic study of the residual stress of cold-formed hollow steel sections, Eng Struct 150 (2017) 986–995, https://doi.org/10.1016/j.engstruct.2017.08.004.
[15] W. Liu, H. Zhang, K. Rasmussen, System reliability-based direct design method for space frames with cold–formed steel hollow sections, Eng Struct 166 (2018) 79–92, https://doi.org/10.1016/j.engstruct.2018.03.062.
[16] R.E. Melchers, A.T. Beck, Structural Reliability Analysis and Prediction, Third., Wiley, Hoboken, NJ, 2018.
[17] T.A. Davison, P.C. Birkemoe, Column Behavior of Cold-Formed Hollow Structural Steel Shapes, Canadian Journal of Civil Engineering 10 (1983) 125–141, https://doi.org/10.1139/l83-014.
[18] L. Wenyu, System Reliability-Based Design of Three-Dimensional Steel Structures by Advanced Analysis, The University of Sydney, 2016 (PhD thesis).
[19] W. Ramberg, W.R. Osgood, Description of stress-strain curves by three parameters, in: Technical Note No. 902, National Advisory Committee For Aeronautics (1943).
[20] G. Shi, X. Zhu, H. Ban, Material properties and partial factors for resistance of high-strength steels in China, J Constr Steel Res 121 (2016) 65–79, https://doi.org/10.1016/j.jcsr.2016.01.012.
[21] L. Gardner, X. Yun, Description of stress-strain curves for cold-formed steels, Constr Build Mater 189 (2018) 527–538, https://doi.org/10.1016/j.conbuildmat.2018.08.195.
[22] M. Loveday, T. Gray, J. Aegerter, TENSTAND - Work Package 1 - Final Report, Tensile Testing of Metallic Materials: A Review, 2004.
[23] EN ISO 6892-1:2019, Metallic Materials. Tensile Testing. Part 1: Method of Test at Room Temperature, 2019.
[24] European standard, Draft prEN 1993-1-1, Eurocode 3 - Design of Steel Structures - Part 1–1: General Rules and Rules for Buildings, CEN/TC 250/SC 3 N 3159, 2020.
[25] L. Gardner, D.A. Nethercot, Numerical modelling of stainless steel structural components-a consistent approach, J STRUCT ENG 130 (2004) 1586–1601, https://doi.org/10.1061/(ASCE)0733-9445(2004)130:10(1586).
[26] R.B. Cruise, L. Gardner, Strength enhancements induced during cold forming of stainless steel sections, J Constr Steel Res 64 (2008) 1310–1316, https://doi.org/10.1016/j.jcsr.2008.04.014.
[27] J.-L. Ma, T.-M. Chan, B. Young, Experimental investigation on stub-column behavior of cold-formed high-strength steel tubular sections, J STRUCT ENG 142 (2016) 4015174, https://doi.org/10.1061/(ASCE)ST.1943-541X.0001456.
[28] J.-L. Ma, T.-M. Chan, B. Young, Cold-formed high strength steel tubular beam-columns, Eng Struct 230 (2021), 111618, https://doi.org/10.1016/j.engstruct.2020.111618.
[29] X. Meng, L. Gardner, Behavior and design of normal- and high-strength steel SHS and RHS columns, J STRUCT ENG 146 (2020) 4020227, https://doi.org/10.1061/(ASCE)ST.1943-541X.0002728.
[30] B. Somodi, B. Kövesdi, Residual stress measurements on cold-formed HSS hollow section columns, J Constr Steel Res 128 (2017) 706–720, https://doi.org/10.1016/j.jcsr.2016.10.008.
[31] A. Kaijalainen, J. Mourujärvi, J. Tulonen, P. Steen, J. Kömi, Effect of ageing on the mechanical properties of cold formed S700 rectangular hollow, IOP Conf Ser Mater Sci Eng 1178 (2021) 12026, https://doi.org/10.1088/1757-899X/1178/1/012026.
[32] M. Sun, J.A. Packer, Direct-formed and continuous-formed rectangular hollow sections — comparison of static properties, J Constr Steel Res 92 (2014) 67–78, https://doi.org/10.1016/j.jcsr.2013.09.013.
[33] B. Somodi, B. Kövesdi, Flexural buckling resistance of cold-formed HSS hollow section members, J Constr Steel Res 128 (2017) 179–192, https://doi.org/10.1016/j.jcsr.2016.08.014.
[34] M. Hayeck, Development of a New Design Method for Steel Hollow Section Members Resistance, 2016 (PhD Thesis).
[35] M. Jandera, L. Gardner, J. Machacek, Residual stresses in cold-rolled stainless steel hollow sections, J Constr Steel Res 64 (2008) 1255–1263, https://doi.org/10.1016/j.jcsr.2008.07.022.
[36] K.J.R. Rasmussen, G.J. Hancock, Design of cold-formed stainless steel tubular members, I: Columns. J STRUCT ENG 119 (1993) 2349–2367, https://doi.org/10.1061/(ASCE)0733-9445(1993)119:8(2349).
[37] Mathworks, Matlab R2020a, 2020.
[38] H. Beer, G. Schulz, The European Column Curves, IABSE Reports of the Working Commissions, 1975.
[39] X. Lan, J. Chen, T.-M. Chan, B. Young, The continuous strength method for the design of high strength steel tubular sections in compression, Eng Struct 162 (2018) 177–187, https://doi.org/10.1016/j.engstruct.2018.02.010.
[40] A. Fieber, L. Gardner, L. Macorini, Design of structural steel members by advanced inelastic analysis with strain limits, Eng Struct 199 (2019), 109624, https://doi.org/10.1016/j.engstruct.2019.109624.
[41] B. Somodi, B. Kövesdi, RUOSTE - Rules On High Strength Steel, Deliverable 2.3, Global Buckling Tests, 2016.
[42] J. Suikkanen, Compression Tests of Ruukki's Double Grade Tubes, Master's Thesis (in Finnish), 2014.
[43] 1090–2 EN, Execution of Steel Structures and Aluminium Structures. Part 2: Technical Requirements for Steel Structures, 2018.